43rd AIAA/ASME/SAE/ASEE Joint Propulsion Conference & Exhibit
8 - 11 July 2007, Cincinnati, OH

AIAA 2007-5796

# DNS Investigation of the Taylor-Culick Flow Stability

F. Chedevergne* and G. Casalis†
*ONERA, 2 av. Edouard Belin, BP 4025, 31 055 Toulouse Cedex, FRANCE*
and J. Majdalani‡
*University of Tennessee Space Institute, Tullahoma, TN 37388*

**In this article, we use a linear, biglobal stability approach to identify the intrinsic instability modes that are responsible for triggering large thrust oscillations in long segmented solid rocket motors (SRMs). Corresponding theoretical predictions compare very favorably with existing experimental measurements acquired from subscale SRM tests. Specifically, the frequency signatures of the thrust oscillations, which form distinct frequency paths, are found to be directly connected to the merging of the intrinsic instabilities of the flow. When these are coupled with the natural acoustic modes of the chamber, large amplitude oscillations are triggered. After undergoing spatial amplification, these oscillations depreciate with the passage of time. To further understand the results obtained from theory, DNS calculations of the rocket motor are performed. These simulations enable us to validate Majdalani's analytical solutions for the oscillatory gas motion. They also provide new physical understanding of the coupling that exists between acoustic pressure modes and intrinsic hydrodynamic instabilities of the Taylor-Culick flowfield. When the intrinsic instability eigenmodes predicted by the biglobal stability approach fall close to the natural frequencies of the chamber, significant amplifications are noted that can lead to appreciable wave steepening. Conversely, when the eigenmodes are sufficiently spaced from the chamber's natural frequencies, no appreciable amplifications are seen. These results agree with the biglobal theory which predicts stable modes when the chamber's length is less than 8 diameters.**

## Nomenclature

| | |
|---|---|
| $\omega_i$ | temporal growth rate |
| $\omega_r$ | circular frequency |
| $\theta$ | azimuthal angle |
| $R$ | radius of the chamber |
| $r$ | dimensionless radial position |
| $R_0$ | radius of the VALDO cold gas facility |
| $s^q_{ac}$ | acoustic part of the physical quantity $q$ : $s^q_{ac} = s^q_{fluc} - s^q_{th}$ |
| $s^q_{fluc}$ | fluctuating part of the physical quantity $q$ |
| $s^q_{th}$ | theoretical evolution of the eigenmode $q$ |
| $t$ | time |
| $V_{inj}$ | injection velocity at the sidewall |
| $x$ | dimensionless axial position |
| $X_e$ | dimensionless length of the truncated domain |

*Subscripts*

| | |
|---|---|
| $()_i$ | imaginary part |

*PhD Student, Aerodynamics and Energetics Modeling Department, Member AIAA.
†Professor and Research Director, Aerodynamics and Energetics Modeling Department, Member AIAA.
‡Jack D. Whitfield Professor of High Speed Flows, Department of Mechanical, Aerospace and Biomedical Engineering, Member AIAA, Fellow ASME.

| | |
|---|---|
| $()_r$ | real part |
| $\_$ | vector |
| $_{ac}$ | acoustic |
| $_e$ | exit plane |
| $_{fluc}$ | fluctuating part |
| $_{th}$ | theoretical part |

# I. Introduction

Large segmented solid rocket motors (SRMs) are known to exhibit thrust oscillations caused by flow-induced pressure fluctuations (Fabignon *et al.*;[1] Ugurtas *et al.*[2]). The problem of understanding and predicting the onset of these oscillations continues to receive attention in the propulsion community, particularly in the framework of the P230 development, the primary booster for the European Ariane 5 launcher (Couton *et al.*[3]). Among the theoretical techniques used to address this problem, hydrodynamic instability theory has long been held as one of the platforms for connecting pressure fluctuations to mean flow instability. The earliest contributions in this direction include those by Varapaev and Yagodkin,[4] Beddini,[5] Lee and Beddini,[6,7] and others. These endeavors rest on the one-dimensional normal mode approach with perturbations in the stream function. Subsequent studies by Casalis and co-workers[8,9] extend the one-dimensional investigations with the addition of experimental measurements and theoretical solutions based on perturbing the primitive variables. The latter are formulated along the lines of the Local Non Parallel (LNP) approach in which all of the non-zero components of the basic flow are retained in the Navier-Stokes equations. Casalis and co-workers[8−11] apply the LNP approach to injection-driven fluid motions in porous channels and tubes using the planar and axisymmetric steady flow profiles of Taylor[12] and Culick,[13] respectively. These are used to mimic the bulk gas motion in slab and circular-port rocket motors. Corresponding experimental facilities that utilize a cold gas simulation are referred to as VECLA and VALDO. Other related studies include those on parietal vortex shedding and its connection to intrinsic instability by Vuillot,[14] Couton *et al.*,[15] Ugurtas *et al.*[16] and Avalon *et al.*[17] The destabilizing effects of headwall injection are also considered by Abu-Irshaid *et al.*[18] in modeling cylindrical solid and hybrid rocket chambers. To overcome the limitations of the LNP approach in modeling the problem in cylindrical, axisymmetric geometry (Griffond *et al.*[10]), a biglobal stability approach has been recently implemented by Chedevergne and Casalis[19,20] and Chedevergne *et al.*[21] By expressing the disturbance amplitudes as a function of two spatial coordinates, radial and axial, the biglobal approach is no longer restricted to a purely exponential form in prescribing spatial amplification or attenuation. At the outset, intrinsic instabilities of the mean flowfield are succinctly identified as the primary source of pressure fluctuations (Chedevergne *et al.*[21]). As shown by Chedevergne and Casalis,[20] biglobal instability predictions compare favorably with live subscale SRM measurements obtained by Prévost *et al.*[22] They also agree satisfactorily with the large collection of data acquired through VALDO, the cold gas experimental facility operated by Avalon and Lambert.[23] Specifically, the unstable frequencies reported in the experiments are found to match the circular frequencies recovered from the biglobal stability analysis. Moreover, the biglobal theory enables us to delineate the frequency paths arising in actual SRMs. In the present study, some points that heretofore had remained obscure are clarified through the use of DNS simulations. Additionally, our results are compared to the closed-form analytical models of Majdalani and co-workers,[24−27] thus helping to validate their asymptotic treatment of the encumbent unsteady wave motion.

The paper is organized as follows. Before exploring the details of the DNS simulation, the first part is dedicated to the linear stability analysis used to capture the intrinsic instabilities of the mean flowfield. In the process, the unresolved issues of this approach are pointed out. Next, the procedure for DNS computations is described. Finally, the verification of the theoretical results by way of comparison to DNS data is carried out.

# II. Biglobal Linear Stability Analysis

## II.A. Mean Flow Model

First we select a model flow to represent the steady-state profile established in a solid rocket motor (SRM). The simulated geometry corresponds to a semi-infinite cylinder of radius $R$. A steady, incompressible fluid is injected through the sidewall at a constant and spatially uniform velocity $V_{inj}$. The flow enters in the radial direction $r$, thus simulating the gas ejection at the burning surface of the propellant. The spatial coordinates and the velocities are made dimensionless with respect to the radius $R$ and the wall-injection velocity $V_{inj}$. Although the Taylor-Culick model corresponds to a semi-infinite cylinder, ours is truncated at $x = X_e$, thus forming a finite chamber that can be practically simulated using a computational code named CEDRE (*Calcul d'Écoulements Diphasiques Réactifs pour l'Énergétique*). This code is developed at ONERA to serve multiple functions, including the calculation of the mean flowfield in a user-designated SRM chamber. CEDRE incorporates innovative techniques, such as the generalized unstructured approach, to offer a unique computational platform for simulating complex problems with reactive multi-physics. The generalized unstructured capability is an original concept that permits the use of cells with an arbitrary number of faces and nodes. Not only does it handle usual structured, unstructured, and hybrid type grids (tetrahedrons, prisms, and pyramids), it also allows for advanced capabilities in grid generation and refinement. More details on the computations can be found in Sec. III.A.

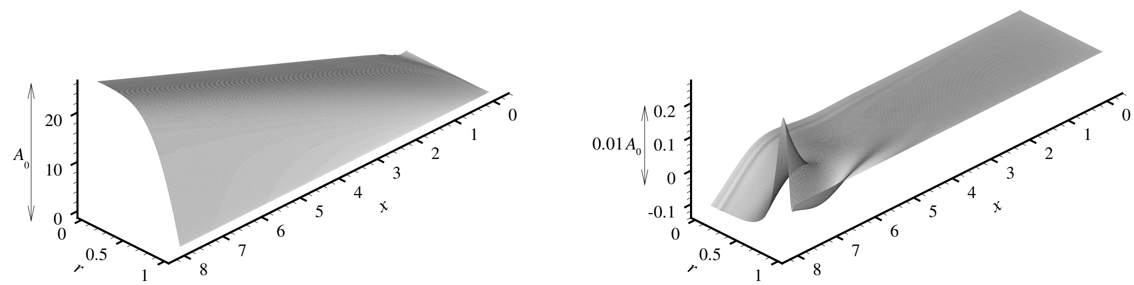


(a) $\bar{U}_x$

(b) $(\hat{u}_x)_r$

**Figure 1. Longitudinal components of the velocities of the basic flow $\bar{U}_x$ and of the perturbation $\hat{u}_x$ (real part). Here the initial amplitude $A$ and time $t$ of Eq. (3) are $t = 0$ and $A = 0.01A_0$.**

Figures 1(a) and 2(a) provide three-dimensional views of the mean axial and radial velocity components computed at a dimensionless $X_e = 8$ and $V_{inj} = 1$ m/s. One notes that this flow closely resembles the Taylor-Culick model[12,13] except in the fore-end region where a boundary layer develops in fulfillment of the no-slip requirement at the headwall (see Chedevergne and Casalis[28]). The CEDRE-based solution is computed in the $(x, r)$ plane assuming axisymmetric, rotational, laminar flow. The agreement obtained between the computed flow and the Taylor-Culick profile confirms the essentially incompressible character of the flow. While a compressible solution for the Taylor-Culick problem has been recently developed by Majdalani,[29] it is not employed here due to the relatively small velocities characterizing our problem. Furthermore, experimental measurements obtained through ONERA's cold gas facility VALDO provide an additional avenue for validation, being in agreement with our model. Note that VALDO uses a cylindrical chamber of radius $R_0 = 0.03$ m made of poral (bronze porous material), thus providing the possiblity to vary $V_{inj}$ from 0.6 m/s up to 2 m/s. The length of the chamber $X_e$ in VALDO can also vary from 11.2 to 22.4. Thus, the injection-based Reynolds number, defined as usual by $Re = \rho R V_{inj}/\mu$, ranges between $1,200$ and $4,000$ in the VALDO facility. Note that the Reynolds number is the only group parameter that remains in the Navier-Stokes equations.

### II.B. Biglobal Fluctuations

The stability analysis is based on a perturbation concept that considers any physical quantity $Q$ to be a superposition of a mean (steady) variable $\bar{Q}$ and a fluctuating, time-dependent part $q$. If solutions exist for

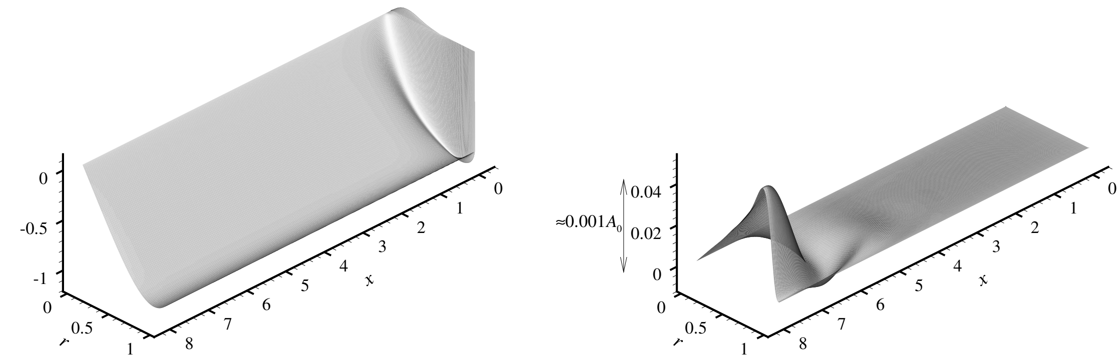


(a) $\bar{U}_r$

(b) $(\hat{u}_r)_r$

**Figure 2. Radial components of the velocities of the basic flow $\bar{U}_r$ and of the perturbation $\hat{u}_r$ (real part).**

$q$, they will be called intrinsic instabilities of the mean flow. The decomposition $Q = \bar{Q} + q$ is introduced into the Navier-Stokes equations which, after some simplifications and cancellations, are split into a linear system of partial differential equations (PDEs). These PDEs prescribe the motion of time-dependent disturbances $q$. They also observe the notion of one-way coupling such that the mean flow can affect the disturbances but not vice versa. In the linearized system, the mean flow and its derivatives define the main coefficients. Next, the biglobal instability theory is applied. Accordingly, any perturbation $q$ may be judiciously expressed as :

$$q = \hat{q}(x,r)e^{i(n\theta-\omega t)} \tag{1}$$

This unsteady variable representation is consistent with the mean flow being dependent on both $x$ and $r$. It is spatially more accurate than one-dimensional approximations in which $\hat{q}$ is taken to be a function of the radial coordinate only. In Eq. (1), $n$ is an integer that denotes the azimuthal wave number, an index that vanishes for strictly axisymmetric disturbances, $\theta$ stands for the azimuthal angle, and $\omega$ represents the complex circular frequency. While its real part $\omega_r$ reproduces the circular frequency of oscillations, its imaginary part $\omega_i$ controls the temporal growth rate.

As we take a first look at this problem, we focus our attention on the axisymmetric models for which $n = 0$. This case is not restrictive because higher tangential modes tend to be less critical from a stability standpoint.

### II.C. Stability Identification Procedure

The use of $n = 0$ enables us to define a stream function $\psi$ for the perturbation. In fact, the linearized Navier-Stokes equations written for the stream function $\psi$ lead to a fourth order PDE $(E)$ in $(x,r)$. This equation can then be solved for $(x,r) \in [0, X_e] \times [0,1]$. As boundary conditions are imposed on the stream function, a suitable outflow condition is formulated at $x = X_e$ following Theofilis[30] and Casalis *et al.*[31] After discretization in the computational domain, $(E)$ is written as a generalized eigenvalue problem $\underline{\underline{\mathcal{A}}}\ \underline{\Psi} = \omega\ \underline{\underline{\mathcal{B}}}\ \underline{\Psi}$. Then, Arnoldi's algorithm is implemented to the extent of generating both problem's complex eigenvalues $\omega$ and their associated eigenfunctions (Golub and Van Loan[32]). The set of complex eigenvalues $\omega$ defines the spectrum of the stability problem. In the interest of clarity, a sample set of complex eigenvalues is showcased in Fig. 3 for $Re = 1975$. It should be noted that for each calculated eigenvalue $\omega$ in Fig. 3, a companion eigenvector $\underline{\Psi}$ is obtained with its components representing the discretized values of the associated eigenfunction $\hat{\psi}(x,r)$. In relation to axial and radial velocity eigenfunctions, one has :

$$\hat{u}_x = \frac{1}{r}\frac{\partial\hat{\psi}}{\partial r} \quad \text{and} \quad \hat{u}_r = -\frac{1}{r}\frac{\partial\hat{\psi}}{\partial x} \tag{2}$$

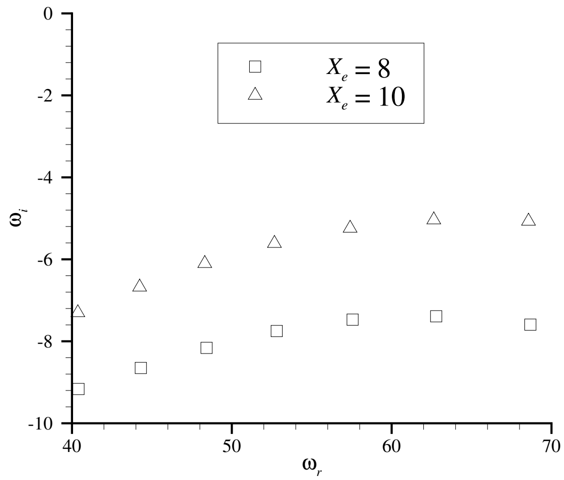


**Figure 3. Set of eigenvalues in the complex $(\omega_r, \omega_i)$ plane for $Re = 1975$. Two cases are shown : $X_e = 8$ (squares) and $X_e = 10$ (triangles).**

The perturbation $q = \hat{q}e^{-i\omega t}$ will therefore contain the essential fluctuating flow ingredients such as $u_x, u_r, p$ and their derivatives; it is referred to as an instability mode, being different for each $\omega$. Once the results of the stability analysis are recast into dimensional quantities (using the constant parameters $R$ and $V_{inj}$), a physical perturbation $q$ for a given mode $\omega = \omega^0$ can be written as :

$$q = A\hat{q}e^{i\frac{V_{inj}}{R}\omega^0 t} = A\left[(\hat{q})_r \cos(2\pi f t) + (\hat{q})_i \sin(2\pi f t)\right]e^{\nu t} \quad \text{with} \quad f = \frac{V_{inj}}{2\pi R}\omega_r^0 \quad \text{and} \quad \nu = \frac{V_{inj}}{R}\omega_i^0 \tag{3}$$

where $\omega^0 = \omega_r^0 + i\omega_i^0$ and $A$ represents the initial amplitude of the perturbation, an initially unknown value. There is no need to specify the intial amplitude $A$ as long as $q$ is a solution of a linear system.

Two major results stemming from the stability analysis can be immediately pointed out. First, we note that the spectrum is discrete. As such, only a discrete set of circular frequencies exists for which unstable disturbances/waves can develop from the main flow. Second, all of the eigenvalues $\omega$ bear a negative imaginary part. This implies that all of the spatially unstable modes will be exponentially damped in time. Their associated eigenfunctions will, however, grow exponentially in the streamwise direction.

The spatial growth of the oscillations is illustrated in Figures 1(b) and 2(b); these present the spatial evolution of the real part of the eigenfunctions $\hat{u}_x$ and $\hat{u}_r$ for the eigenvalue $\omega^0 = 40.409 - 9.164i$ and $X_e = 8$. Without having been prescribed in the theory (see Eq. (1)), the three-dimensional plots clearly show a strong (exponential-like) amplification in the streamwise direction. Thus for a given eigenvalue, two counteracting mechanisms are seen to coexist : a temporal decay affecting the perturbations as time elapses and a spatial growth in the perturbed amplitudes as wave propagation intensifies in the longitudinal direction $x$.

### II.D. Mode Dependence on Motor Length

So far, the character of the instability modes has provided a new physical understanding of the mechanisms that drive the thrust oscillations in SRMs. As confirmed by Chedevergne and Casalis,[20] the frequency paths recovered in all subscale and full scale SRMs are caused by the merging of the instability modes of the flow (also called intrinsic instabilities). The merging is attributed to the strong coupling between the stability modes and the natural acoustic frequencies of the motor. The instability modes are excited and then amplified by the acoustic sources. After inception, they undergo temporal depreciation as predicted theoretically. However, despite the new physical insight gained from linear stability analysis toward elucidating the origination of the thrust oscillations, a question remains unresolved. As one may infer from Fig. 3, the eigenvalues appear to depend on the length of the domain $X_e$. So by changing the length of the domain, a shift in complex eigenvalues is detected despite the invariance of the mean flow. Given no established explanation for such behavior, it may be speculated that the size dependence is a spurious artifact of the numerical procedure, thus calling into question the whole validity of the stability analysis. To better understand this sensitivity to $X_e$, an independent approach is resorted to, specifically, that of Direct Numerical Simulation (DNS).

## III. Direct Numerical Simulation

As alluded to earlier, we have performed extensive DNS computations with the use of ONERA's code known as CEDRE. The space discretization in CEDRE is based on a finite volume approach that employs an upwind Roe scheme with a second order extension (MUSCL scheme with Van Leer limiter). A complete description of the code is given by Chevalier *et al.*[33] and more specific information concerning code validation for rocket motor simulations may be found in an excellent survey by Vuillot *et al.*[34]

For the present study, laminar Navier-Stokes computations are carried out. In the interest of establishing realistic baseline cases, the characteristic length and velocity are chosen to match those of Avalon and Lambert[23] in their VALDO facility. So in the DNS input file, we use a chamber radius of $R = R_0 = 0.03$ m and an injection velocity of $V_{inj} = 1$ m/s.

Four meshes are successively tested to the extent of establishing grid independence. Our sample results for $X_e = 8$ are performed with a grid that is composed of $301 \times 161$ nodes (for $X_e = 10$ the grid is composed of $351 \times 161$ nodes such that the thickness of the cells at the headend is conserved compared to case $X_e = 8$). Furthermore, cosine repartition is employed such that the thickness of the cells on the boundaries is refined down to approximately 3 $\mu$m.

### III.A. Computing the Mean Flow

An implicit time scheme is used with a fixed value of the Courant-Friedricks-Levy (CFL) number. This number represents, in characteristic grid spacing, the distance that a sound wave would travel in a single time step. Using CFL = 10, steady-state runs are conducted for the purpose of computing the basic flow components that are needed for the linear stability calculations. While it is possible to use the Taylor-Culick approximation, we opt for the computed solution because of its ability to satisfy the headwall boundary condition. Once the computations are confirmed to have reached a converged state, the steady flow is retrieved in discrete fashion and fed into the stability code, thus supplanting the Taylor-Culick formula.

In principle, a no-slip condition at $x = 0$ is essential for a viscous fluid, a condition that is not observed by the Taylor-Culick profile. Nonetheless, the boundary layer that develops at $x = 0$ only affects the flow in the vicinity of the headwall. In this neighborhood (see Figs. 1(b) and 2(b)), the fluctuations are nearly zero, and so the use of the Taylor-Culick solution continues to be a suitable approximation : it leads to practically identical stability results (in tems of circular frequency $\omega_r$). For further detail on this issue, the reader may refer to Chedevergne and Casalis.[28]

### III.B. Unsteady Calculations

To compute the unsteady field, an explicit time scheme is used with a time step of $\Delta t = 5 \times 10^{-9}$ s. The corresponding maximum CFL number is less than 1. Since the main purpose of this simulation is to verify the results obtained from stability theory, the strategy is to superimpose, at the initial time, an instability mode $\omega = \omega^0$, extracted for example from Figs. 1(b) and 2(b), where $\omega^0 = 40.409 - 9.164i$, on the DNS calculated basic flow, illustrated in Figs. 1(a) and 2(a). The initial time $t$ and amplitude $A$ of Eq. (3) are chosen as $t = 0$ s and $A = 0.01A_0$, where $A_0$ is the peak value attained by the longitudinal component $\bar{U}_x$ of the mean flow. It may be important to note that the pressure perturbation of the stability mode $\omega = \omega^0$ is not superimposed on the pressure distribution of the mean flow, being very small in amplitude. At first glance, the superposition process may appear to be simple. In actuality, the overlapping of the mean and unsteady components proves to be quite challenging. It requires careful grid projections that do not introduce artificial errors. It also requires special attention to be paid to the boundary conditions. Once the superposition is resolved, the unsteady DNS computations are started. The origin of time is set at $t = 0$ s. At $t = 0.02$ s, that is to say after $4,000,000$ iterations, our computer runs are stopped and their output exported. Signals from different virtual sensors (placed to cover the flow in the entire chamber) are extruded and analyzed.

Before leaving this subject, it may be useful to remark that other strategies exist for exploring the character of oscillations in similar flowfields. For example, Apte and Yang[35,36] introduce a white noise or an acoustic excitation to perform LES calculations that can suitably capture the triggered instabilities.

### III.C. Three Representative Cases

Using the strategy described above, several representative computations are performed by changing the eigenmode introduced at $t = 0$ s or the length of the chamber $X_e$. In this article, three benchmark cases are chosen at fixed values of $R$ and $V_{inj}$. The first two enable us to capture the effect of changing $X_e$, and the third, to explore the steepening behavior that emerges from the instability mode being close to the main chamber's acoustic frequency.

- Case 1 : corresponds to the behavior of the oscillatory mode $\omega^0 = 40.409 - 9.164i$ in a chamber of length $X_e = 8$. The corresponding frequency is $f = 214$ Hz.
- Case 2 : corresponds to the behavior of the oscillatory mode $\omega^0 = 40.367 - 7.302i$ in a chamber of length $X_e = 10$. The corresponding frequency is $f = 214$ Hz.
- Case 3 : corresponds to the behavior of the oscillatory mode $\omega^0 = 68.679 - 7.594i$ in a chamber of length $X_e = 8$. The corresponding frequency, $f = 364$ Hz, is nearly identical to the first acoustic mode in the chamber, specifically, $f_{ac} = 363$ Hz.

The essential difference between the first two cases is limited to the computations being carried out for slightly longer chambers. In Fig. 3, one can clearly see that the mode $\omega = 40.409 - 9.164i$, calculated for $X_e = 8$, shifts to $40.367 - 7.302i$ when the length is increased to $X_e = 10$. Physically, the two modes are the same, being the lowest for the given geometry.

For the two chamber lengths, $X_e = 8$ and 10, the acoustic frequencies are 291 Hz and 363 Hz, respectively. For Cases 1 and 2, the frequency of the intrinsic disturbance is $f = V_{inj}\omega_r^0/(2\pi R_0) = 214$ Hz; it is therefore lower than the natural acoustic mode frequencies. Because of this disparity in acoustic versus intrinsic instability frequencies, on expects the perturbations to exhibit linear oscillations. In contrast to the first two cases, Case 3 consists of an instability mode with frequency that locks on the first acoustic mode. At the outset, one expects nonlinear interactions to be eminent. These three cases are situated side-by-side on Fig. 4, thus displaying both the acoustic and intrinsic stability mode frequencies with respect to the chamber length $X_e$.

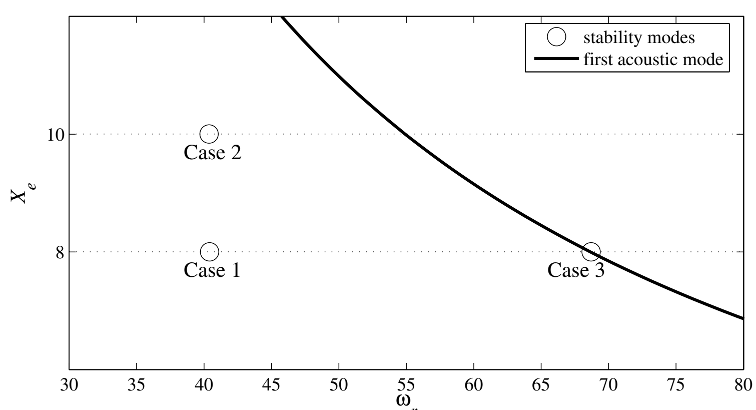


**Figure 4. Sketch representing the three benchmark cases.**

# IV. Results and Discussion

## IV.A. Case 1

As stated in Sec. III.C, the mode $\omega^0 = 40.409 - 9.164i$ in Case 1 is superimposed on the basic steady flow over a segment that is delineated by $X_e = 8$. At $t = 0$ s, only the real parts of $(\hat{u}_x)_r$ and $(\hat{u}_r)_r$ are added to $\bar{U}_x$ and $\bar{U}_r$, respectively. Using $s^q_{fluc}$ to denote a fluctuating DNS quantity, this oscillatory part can be calculated from the difference between the signal of a virtual DNS sensor placed at a predetermined station in the chamber and its corresponding steady flow component. Any signal $s^q_{fluc}$ can therefore be compared to its theoretical evolution $s^q_{th}$, expressed through Eq. (3). The latter reproduces the temporal behavior of the fluctuation $q$ directly from the biglobal stability analysis.

Results are shown in Fig. 5 that compare the DNS signals $s^q_{fluc}$ and their corresponding theoretical evolutions $s^q_{th}$. The fluctuations are displayed, side-by-side, for $q = u_x$ and $q = u_r$, at three different locations. As one may infer from Figs. 5(b), 5(d), and 5(f), an excellent agreement may be said to exist between DNS and biglobal stability solutions for the radial velocity component : $s^{u_r}_{fluc} \approx s^{u_r}_{th}$. A notable exception may be seen for the third sensor in Fig. 5(f), where the signal $s^{u_r}_{fluc}$ is jarred by spurious noise. Notwithstanding the numerical artifact, one may argue that the general behavior in Fig. 5(f) still corresponds to the theoretical modal evolution $s^{u_r}_{th}$. In fact, the spatial perturbation $(\hat{u}_r)_r$ introduced at $t = 0$ s in the DNS code evolves computationally in parallel to the theoretically predicted pattern, thus implying a faithful agreement between DNS and biglobal stability predictions for not only $(\hat{u}_r)_r$ but also for $(\hat{u}_r)_i$, $\omega_r$ and $\omega_i$. It is gratifying that both the circular frequency $\omega_r = 40.409$ and the temporal growth rate $\omega_i = -9.164$ are identically recovered by the DNS solution.

With respect to the axial velocity component, the agreement between DNS and theory, while acceptable in Fig. 5(a), deteriorates in Figs. 5(c) and 5(e). One may hence argue that $s^{u_x}_{fluc} \neq s^{u_x}_{th}$. Upon closer examination and guided by the fact that $s^{u_r}_{fluc} = s^{u_r}_{th}$ is verifiable, we posit that there must be a part of $s^{u_x}_{fluc}$ that corresponds to $s^{u_x}_{th}$. The remaining disparity, specifically, $s^{u_x}_{fluc} - s^{u_x}_{th}$, may be attributed to acoustic coupling in the chamber. We thus define $s^{u_x}_{ac} = s^{u_x}_{fluc} - s^{u_x}_{th}$, recognizing that $s^{u_r}_{ac} \approx 0$.[a]

### *IV.A.1. Vortico-Acoustic Boundary Layer*

In the context of a porous chamber with sidewall injection, several explicit solutions exist to describe the oscillatory acoustico-vortical waves driven by pressure fluctuations (see Majdalani and co-workers[24,27]). Only the basics of the approach used by Majdalani are revisited here. Accordingly, a perturbation $q$ above the mean flow $\bar{Q}$ is introduced to the extent of linearizing the compressible Navier-Stokes equations before seeking a solution via asymptotics. Several perturbation methods are utilized including WKB, composite scales, and generalized scales. The mean flow is taken to be of the Taylor-Culick form, although Majdalani has generalized the time-dependent formulation to accommodate an arbitrary mean flow profile.[26,27] When using Taylor-Culick's profile, Majdalani's solution is expected to be valid everywhere except in the close vicinity of the headwall. This particular limitation remains secondary given that fluctuations near the headwall are so small that they cannot be of any material consequence.

In Majdalani's work, the temporal perturbation $q$ is divided into two complementary parts : $q = \breve{q} + \tilde{q}$. While $\breve{q}$ is an irrotational compressible wave that is pressure driven, $\tilde{q}$ is an incompressible rotational wave that is vorticity driven. These fluctuations are referred to as mass-like or force-like, sound or vorticity disturbance modes by Chu and Kovásznay.[37] The superposition itself is granted by the Helmholtz decomposition theorem. Accordingly, an arbitrary vector function can be split into two parts : an irrotational component that is expressible by the gradient of a scalar function, and a rotational part that is collapsible into a curl of a vector function. In our problem, $\breve{q}$ stands for the acoustic wave solution that is dominated by longitudinal oscillations in an elongated chamber with no mass addition. This leaves $\tilde{q}$ as the correction needed to account for sidewall mass addition, driven by the basic flow $\bar{Q}$, that enters the chamber perpendicularly to the longitudinal plane wave $\breve{q}$. As noted by Griffond,[38] $\tilde{q}$ is the agent that controls the vortico-acoustic

[a]As shown in Sec. IV.A.1, the radial acoustic velocity component $\breve{u}_r$ is zero and $\tilde{u}_r$ is of order $M$ compared to $\tilde{u}_x$. $M$ is about 0.0027 in our cases and so $s^{u_r}_{ac}$ is almost zero.

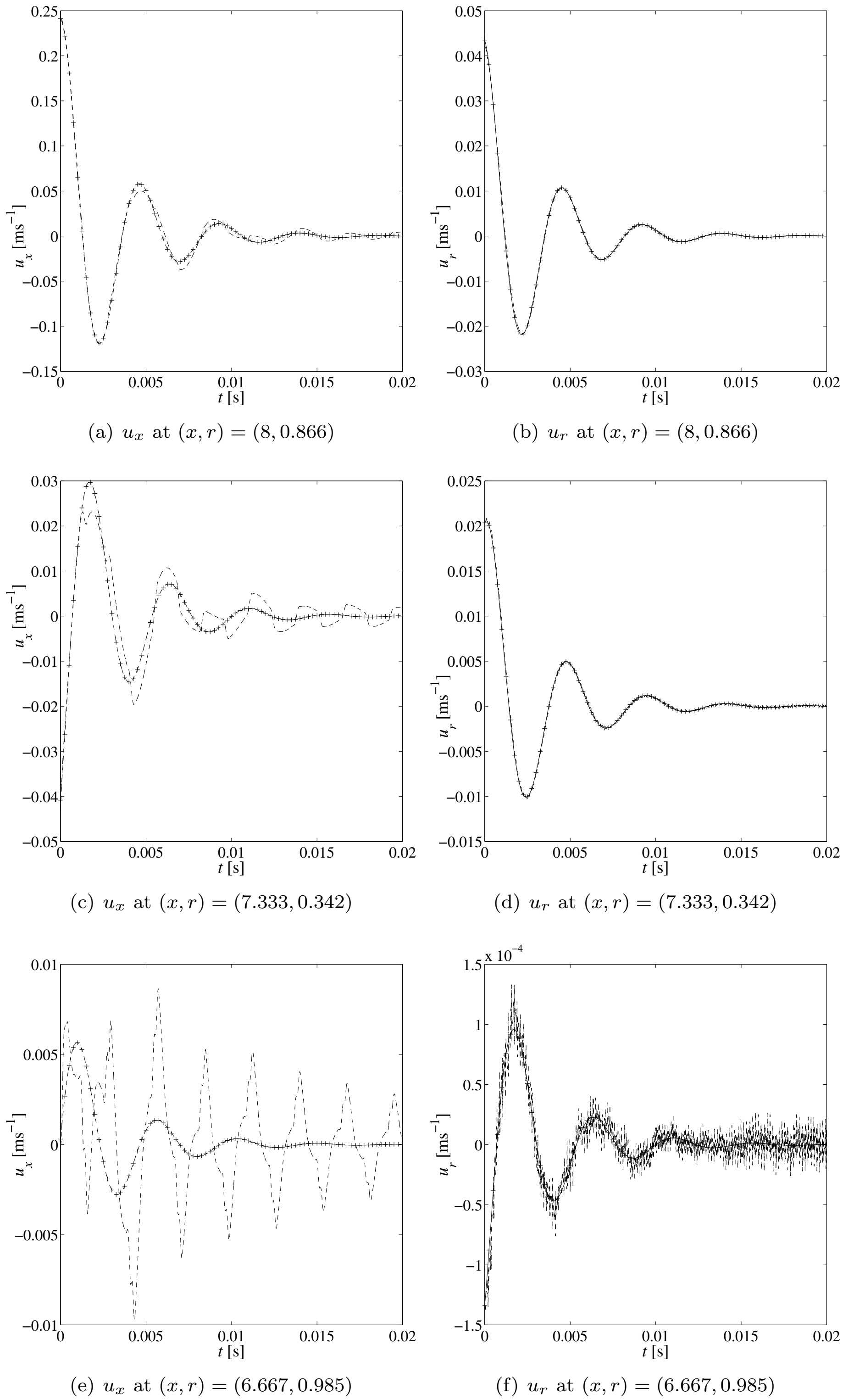


(a) $u_x$ at $(x, r) = (8, 0.866)$

(b) $u_r$ at $(x, r) = (8, 0.866)$

(c) $u_x$ at $(x, r) = (7.333, 0.342)$

(d) $u_r$ at $(x, r) = (7.333, 0.342)$

(e) $u_x$ at $(x, r) = (6.667, 0.985)$

(f) $u_r$ at $(x, r) = (6.667, 0.985)$

**Figure 5. Case 1. Comparisons between the fluctuating part of the signal of three sensors $s^q_{fluc}$ (dashed line) and the theoretical evolutions $s^q_{th}$ (solid line with +) given by Eq. (3).**

boundary layer, often referred to simply as acoustic layer. It follows that, for the sound wave, one may put :

$$\left\{ \begin{array}{l} \breve{p}(x, t^*) = \cos(\omega_m x)\, e^{-i\omega_m t^*} \\ \\ \underline{\breve{u}}(x, t^*) = i \sin(\omega_m x)\, e^{-i\omega_m t^*}\, \underline{e}_x \end{array} \right. \tag{4}$$

where $\breve{p}$ and $\breve{\underline{u}}$ are the pressure and velocity fluctuations of the longitudinal plane wave and $t^* = ta_0/R$ is normalized by the characteristic time that an acoustic disturbance will take to cross the radius of the chamber. Given closed-open acoustic conditions in both DNS and stability calculations, one may use a circular frequency of $\omega_m = (m - \frac{1}{2})\pi/X_e$, where $m \in \mathbb{N}^*$. Then, based on Majdalani's work, the boundary-driven vorticity wave for a flow $\underline{Q}$ characterized by $\psi(x,r) = xF(r)$ can be generalized into :

$$\left\{ \begin{array}{l} \tilde{u}_x = -i\left(\dfrac{F}{F_0}\right) e^{[\zeta - i(\omega_m t^* + \Phi)]} \quad ; \quad F_0 \equiv F(1),\ F_0' \equiv F'(1) \\ \\ \tilde{u}_r = -\dfrac{M}{r}\left(\dfrac{F}{F_0}\right)^3 e^{[\zeta - i(\omega_m t^* + \Phi)]} \end{array} \right. \tag{5}$$

where $M = V_{inj}/a_0$ is the wall injection Mach number. Using Majdalani's generalized-scaling technique, $\zeta(r)$ and $\Phi(r)$ may be written at order $Re^{-1}$ :

$$\left\{ \begin{array}{l} \zeta(r) = \xi \displaystyle\int_1^r x^3 F^{-3}(x)dx \\ \Phi = S_m \left[\displaystyle\int_1^r \left(xF^{-1} - 4Re^{-1}xF^{-2}\right) + \frac{3}{2}Re^{-1}\left(r^2F^{-2} - F_0^{-2}\right)\right] \end{array} \right. \tag{6}$$

where

$$\xi = \frac{S_m^2}{Re} = \frac{\omega_m^2}{M^2 Re} \quad ; \quad S_m = \frac{\omega_m}{M} \quad ; \quad Re = \frac{V_{inj}R}{\nu} \tag{7}$$

The arbitrary function $F$ can be taken to be :

$$F(r) = \left\{ \begin{array}{ll} r^2(2 - r^2) & 10 < Re < 100 \\ \sin\left(\dfrac{1}{2}\pi r^2\right) & Re \geq 100 \end{array} \right. \tag{8}$$

The Taylor-Culick flow is thus a special case for which $F = \sin\theta$, $F_0 = 1$, $F_0' = 0$, and $\theta = \frac{1}{2}\pi r^2$. The corresponding solution reduces to :

$$\left\{ \begin{array}{l} \tilde{u}_x = -i\sin\theta\sin\left(\omega_m x\sin\theta\right) e^{[\zeta - i(\omega_m t^* + \Phi)]} \\ \\ \tilde{u}_r = -\dfrac{M}{r}\sin^3\theta\cos\left(\omega_m x\sin\theta\right) e^{[\zeta - i(\omega_m t^* + \Phi)]} \\ \\ \zeta = -\dfrac{\xi}{\pi^2}\left[\csc\theta - 1 + \theta\cot\theta\csc\theta + I\left(\frac{1}{2}\pi\right) - I\left(\theta\right)\right] \\ \\ \Phi = \dfrac{S_m}{\pi}\ln\tan\left(\frac{1}{2}\theta\right) + \dfrac{S_m}{\pi Re}\left[4\cot\theta + 3\left(\theta\csc^2\theta - \frac{1}{2}\pi\right)\right] \\ \\ I\left(\theta\right) = \theta + 2\displaystyle\sum_{k=1}^{\infty}\frac{\left(1 - 2^{1-2k}\right)}{\left(2k+1\right)\pi^{2k}}\left(\sum_{j-1}^{\infty}\frac{1}{j^{2k}}\right)\theta^{2k+1} = \theta + \frac{1}{18}\theta^3 + \frac{7}{1800}\theta^5 + \frac{31}{105840}\theta^7 + ... \end{array} \right. \tag{9}$$

A simpler closed-form expression may be obtained, as shown by Majdalani and Van Moorhem,[24] using the concept of composite scales. The technique is a variant of multiple scales theory that applies to the treatment of problems with nonlinear scales (see also Majdalani[26,39]). At the outset, one may use a practically equivalent expression to Eq. (9), namely :

$$\left\{ \begin{array}{rcl} \zeta &=& -\xi\left[\dfrac{\eta(r)r^3}{F^3} - \dfrac{\eta(1)}{F_0^3}\right] = -\xi\dfrac{\eta(r)r^3}{\sin^3\theta} \quad ; \quad \eta(r) = \dfrac{1 - r}{1 + \frac{3}{2}(1-r)^{\frac{3}{2}}\left[\frac{1-r}{r} - \frac{3}{2}\ln r\right]} \\ \Phi &=& S_m\displaystyle\int_1^r \frac{x}{F}dx + \frac{S_m}{Re}\left[\frac{\eta(r)r}{F^3}(3rF' + 2F) - \frac{\eta(1)}{F_0^3}(3F_0' + 2F_0)\right] \\ &=& \dfrac{S_m}{\pi}\ln\tan\left(\frac{1}{2}\theta\right) + \dfrac{2S_m}{Re}\dfrac{\eta(r)r}{\sin^2\theta}\left(1 + \dfrac{3\theta}{\tan\theta}\right) \end{array} \right. \tag{10}$$

The vortico-acoustic boundary layer that accompanies this solution is characterized by Majdalani.[25] It is confirmed by Griffond[38] and Wasistho *et al.*[40] to be suitable up to the point where hydrodynamic instability waves become relatively large.

Equations (4-10) provide an effective framework for approximating the vortico-acoustic modes in a porous chamber, thus taking into account the effect of the mean flow $\bar{Q}$. The minor weakness in not securing the headwall velocity adherence requirement has almost no bearing on the overall accuracy. It remains of little consequence, particularly when the analytical solution is compared to DNS calculations. It should be noted that while the biglobal instability waves have short wavelengths and slow propagation speeds (that continually vary), the vortico-acoustic waves exhibit large wavelengths and propagation speeds that are comparable to the speed of sound. Since these modes evolve over widely dissimilar spatial and temporal scales, their superposition is permitted.

#### *IV.A.2. Decomposition of Acoustic Modes via Least Squares*

Assuming that the vortico-acoustic perturbations $s^q_{ac}$ exhibited by the DNS output is a linear combination of acoustic modes, we use $\{A_m\}$ to denote the corresponding coefficients. These coefficients are the amplitudes of each acoutic mode given by Eqs. (4-10). To find the correct combination, we focus on the pressure signal $s^p_{fluc}$. Any signal $s^p_{fluc}$ is mainly prescribed by the acoustic waveform $\breve{p}$, because $\hat{p}$ and $\tilde{p}$ are negligible by comparison. While the pseudopressure $\tilde{p}$ that accompanies the boundary-driven vorticity wave is well known to be of higher order in the Mach number, the pressure fluctuation due to intrinsic instability is also weak, especially in the forward segment of the simulated SRM chamber (where $x$ is small). We essentially have $s^p_{fluc} \approx s^p_{ac}$.

Thus given that the pseudosound is zero ($\tilde{p} \approx 0$), it is helpful to estimate the coefficients $\{A_m\}$ of the decomposition of the vortico-acoustic signal by considering a number, say $N = 100$, of analytical acoustic modes for the pressure based on the signals $s^p_{fluc}$. For a given sensor, a linear system involving the coefficients $\{A_m\}$ is obtained from the equality at each time between the signal $s^p_{fluc}$ and the combination of the first 100 acoustic modes. Using the method of least squares, the coefficients are determined. This process can be applied to $s^{u_x}_{ac} = s^{u_x}_{fluc} - s^{u_x}_{th}$, leading to rather similar combination. Once the decomposition is completed, the coefficients $\{A_m\}$ are used to calculate the acoustic combination anywhere in the chamber and compare it to the signals $s^p_{ac}$ and $s^{u_x}_{ac}$. Since the acoustic modes of Eqs. (4-10) are only oscillating in time and not diminishing, an artificial analytical function of viscosity $F_\mu(t)$ [b] is multiplied by the combination of acoustic modes to mimic the process of viscous dissipation that causes acoustic wave attenuation. Note that the function $F_\mu(t)$ is used for all the sensors irrespective of the physical quantity $q$ at hand.

Finally, a comparison between $s^p_{ac}$ for Sensor 22 and the combination of acoustic modes is shown in Fig. 6(a). Since a combination of acoustic modes can reproduce the signals $s^p_{ac}$ at any location in the chamber, $s^p_{ac}$ is in fact the acoustic part of the pressure signal. In Fig. 6(b), the coefficients $\{A_m\}$ are plotted with respect to the mode number $m$ for the first 20 modes. Clearly, $A_m \approx \frac{1}{m^2}$ and the combination found corresponds to a harmonic distribution of acoustic modes.

The same coefficients $\{A_m\}$ obtained through least squares are subsequently used to evaluate the acoustic longitudinal velocity fluctuations. The results are shown in Figs. 7(a), 7(b) and, 7(c). This plot illustrates, at three sensor locations, the vortico-acoustic contribution retrieved from DNS data and the analytical prediction obtained by linearly summing 100 vortico-acoustic modes.

It is evident in Fig. 7 that the set of coefficients $\{A_m\}$ enables us to reproduce, as accurately as possible, the combination of acoustic modes that are derived from the DNS calculations. This excellent agreement between DNS and analytical modeling helps to establish both the relevance and accuracy of Majdalani's approximation for the vortico-acoustic modes.

---

[b] $F_\mu(t)$ is adjusted to match the viscous dissipation observed in the signals. One finds $F_\mu(t) = F^0_\mu e^{-2.3\frac{V_{inj}t}{R_0}}$. $F^0_\mu$ is a constant which depends on the signal quantity $q$ at hand, *i.e.* $u_x$ or $p$.

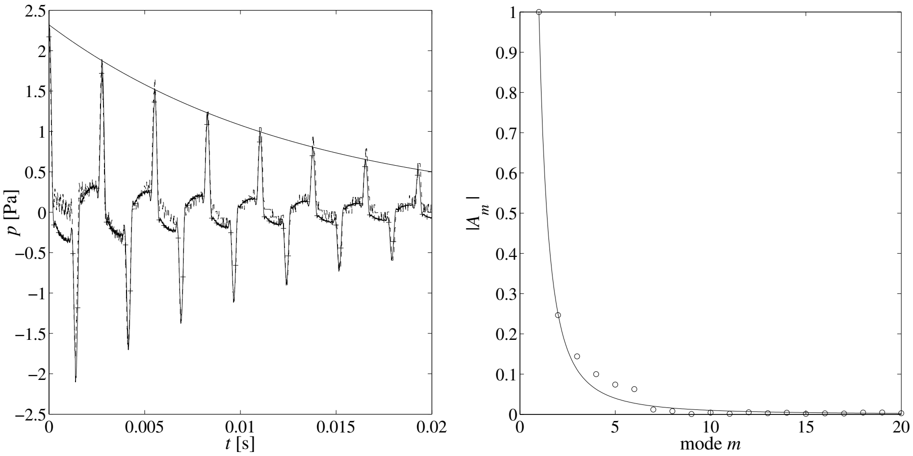


(a) $p$ (b) $A_m$

**Figure 6. Case 1. Fig. 6(a) presents the comparison between the signal $s_{ac}^{p}$ (dashed line) and the combination of 100 acoustic modes (solid line with +) for a sensor located at $(x, r) = (6.667, 0.985)$. The function $F_\mu$ (solid line) stands for the envelope of the combination. The circles in Fig. 6(b) show the values $\{A_m\}$ of the coefficients with respect to the mode number $m$. They are compared to the line $1/m^2$.**

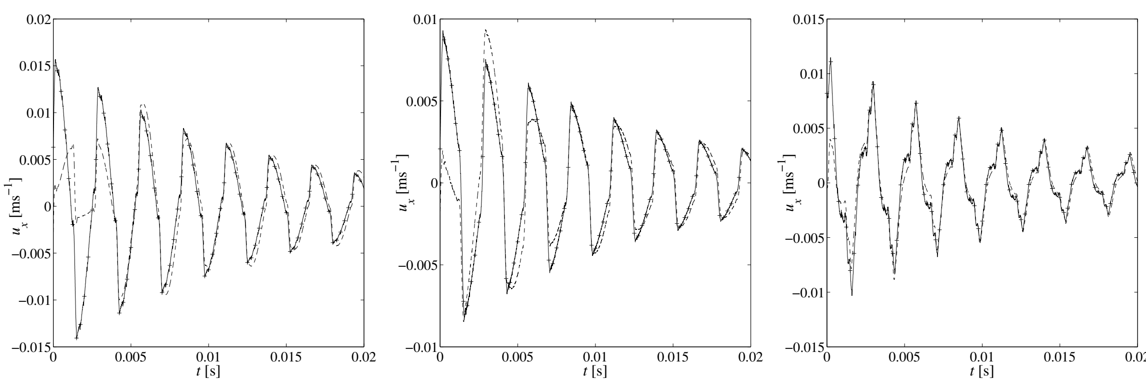


(a) $u_x$ at $(x, r) = (8, 0.866)$ (b) $u_x$ at $(x, r) = (7.333, 0.342)$ (c) $u_x$ at $(x, r) = (6.667, 0.985)$

**Figure 7. Case 1. Comparisons between the signals $s_{ac}^{u_x}$ (dashed lines) of three sensors and the combination of 100 acoustic modes (solid lines with +) given by the coefficients $\{A_m\}$. The envelope of the theoretical acoustic signals is related to the function $F_\mu$.**

Before leaving this baseline case, it may be instructive to note that by choosing $X_e = 8$ and $\omega^0 = 40.409 - 9.164i$, the DNS model has been shown to faithfully reproduce both circular frequency $\omega_r$ and temporal damping rate $\omega_i$ predicted by the biglobal stability analysis. The separate contributions of boundary-driven vortico-acoustic disturbances are found to contain a linear distribution of acoustic modes that are well predicted by Majdalani's analytical solution. Despite the excellent agreement obtained heretofore, it remains to be established whether reconciliation between theory and simulation will continue to hold, specifically, in predicting the temporal growth rate $\omega_i$ as the length of the chamber is changed.

### IV.B. Case 2

The instability mode in question is $\omega^0 = 40.367 - 7.302i$. This is essentially the same mode as in Case 1, *i.e.* $\omega^0 = 40.409 - 9.164i$, except that it has shifted slightly. Its temporal growth rate has decreased as a result of increasing the domain of investigation from $X_e = 8$ to $X_e = 10$ (see Fig. 3). As usual, only the real parts $(\hat{u}_x)_r$ and $(\hat{u}_r)_r$ of the mode $\omega^0 = 40.367 - 7.302i$ are added to $\bar{U}_x$ and $\bar{U}_r$ in the DNS calculations at $t = 0$ s. The method of least squares is then used to calculate the coefficients $\{A_m\}$ of the first 100 acoustic modes of the vortico-acoustic signal which corresponds to a pressure signal $s_{ac}^{p}$. The function $F_\mu(t)$ is also used to mimic the effects of viscous dissipation.

Figure 8 compares the key flow ingredients using DNS and stability calculations at a sensor location $(x, r) = (8, 0.809)$. The agreement is excellent in Fig. 8(a) showing that $s^{u_r}_{fluc} = s^{u_r}_{th}$. As one may infer

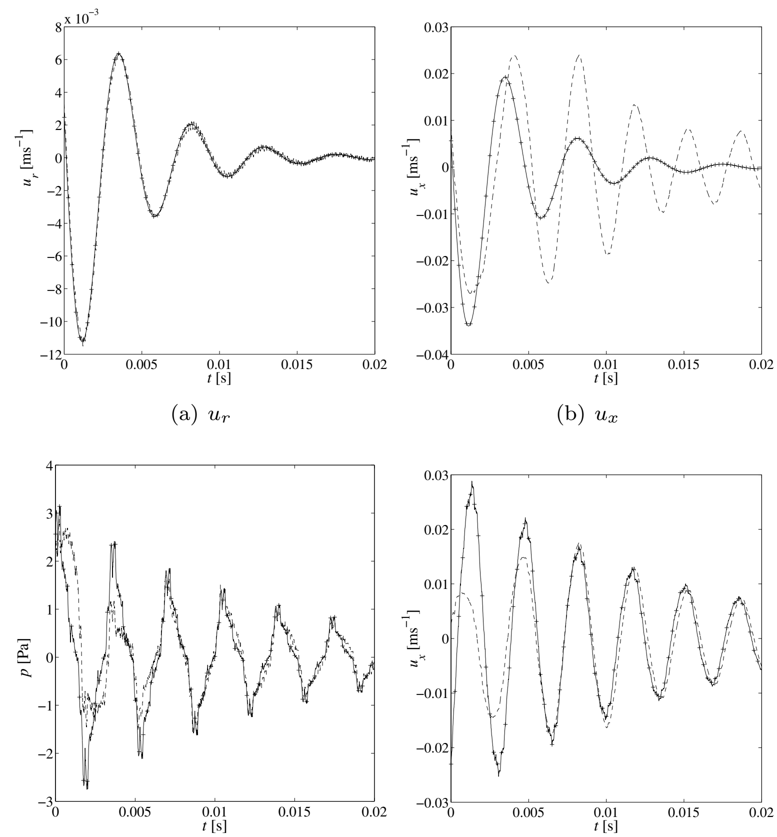


(a) $u_r$ (b) $u_x$

(c) $p$ (d) $u_x$

**Figure 8. Case 2. The signals are originating from a sensor located at $(x, r) = (8, 0.809)$. Parts 8(a) and 8(b) compare signals $s^{u_x}_{fluc}$ and $s^{u_r}_{fluc}$ (dashed lines) and their respective theoretical evolutions $s^{u_x}_{th}$ and $s^{u_r}_{th}$ (solid lines with +). Parts 8(c) and 8(d) compare signals $s^{p}_{ac}$ and $s^{u_x}_{ac}$ (dashed lines) and a combination determined by the coefficients $\{A_m\}$ of the first 100 acoustic modes (solid lines with +) calculated from a pressure signal $s^{p}_{fluc}$ at the section $x = 1$.**

from Fig. 8(a), it is gratifying that both $\omega_r$ and $\omega_i$ anticipated from the stability analysis are confirmed in the DNS calculations. We conclude, in particular, that the evolution of the temporal growth rate $\omega_i$ with respect to $X_e$ is not a spurious numerical artifact. Being confirmed by both DNS and stability models, we rule out the possibility of ill-conditioning in the numerical procedure for computing the stability eigenvalues. The shift in eigenvalues may be ascribed to the increase in $X_e$. This increase leads to higher axial velocities within the domain of investigation. Of course, there may be other factors that promote the dependence of $\omega_i$ on $X_e$. As $X_e$ continues to increase, $\omega_i$ will tend toward zero. It is possible for the temporal growth rate to switch sign for sufficiently long domains, specifically, for $X_e = 16$. Switching sign will cause the associated eigenmode to become temporally unstable, hence leading to significant change in the mean flow, specifically, to turbulence.

Figure 8(b) illustrates the difference that exists between $s^{u_x}_{fluc}$ and $s^{u_x}_{th}$. In Case 1 the difference is due to the acoustic modes that develop in the chamber. Using the results of the least squares method, *i.e.* the coefficients $\{A_m\}$, the pressure signal $s^{p}_{ac} \approx s^{p}_{fluc}$ is compared to the combination of the first 100 acoustic modes given by Eqs. (4-10) in Fig. 8(c). Additionally, the coefficients $\{A_m\}$ are used to calculate the acoustic part of the longitudinal velocity, then compared to $s^{u_x}_{ac} = s^{u_x}_{fluc} - s^{u_x}_{th}$. The good agreement obtained in Fig. 8(d) is due, in part, to the relevance of the combination of analytical acoustic modes found by Majdalani.

### IV.C. Case 3

So far we have seen that the mode $\omega^0 = 40.409 - 9.164i$, obtained for $X_e = 8$, shifts to $\omega^0 = 40.367 - 7.302i$ when the length of the domain is increased by one diameter. In both cases, the real frequency of the eigenmodes (40.4 rad/s) corresponds to $f = 214$ Hz. The natural acoustic frequencies of the chamber may be calculated from $f_{ac} = a_0/(4RX_e)$ to find $f = 363$ Hz and 291 Hz for chambers with $X_e = 8$ and 10, respectively. To explore the possible coupling between vortico-acoustic and intrinsic instabilities, we consider a stability mode that either matches or falls close to the chamber's acoustic frequency. In this vein, we consider the mode $\omega^0 = 68.679 - 7.594i$ calculated for $X_e = 8$. Its actual frequency of $f = 364$ Hz is nearly equal to the first natural acoustic mode, $f_{ac} = 363$ Hz. At $t = 0$ s, this mode is superimposed on the basic flow as DNS calculations are initiated.

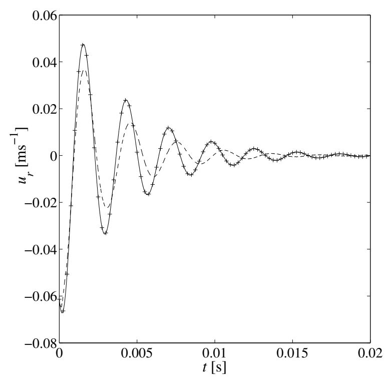


(a) $u_r$ at $(x, r) = (8, 0.866)$

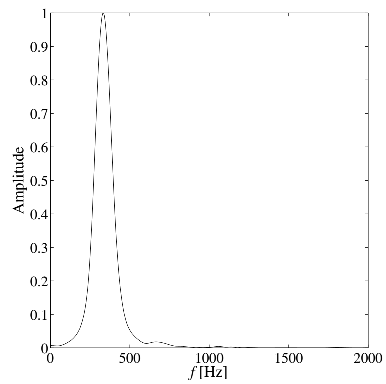


(b) FFT

**Figure 9. Case 3. Part. 9(a) compare the signal $s^{u_r}_{fluc}$ (dashed line)and the theoretical evolution (solid line with +) for the sensor located at $(x, r) = (8, 0.866)$. Part. 9(b) provides the FFT signal obtained from $s^{u_r}_{fluc}$.**

Figure 9(a) shows that the signal $s^{u_r}_{fluc}$ does not match the theoretical evolution $s^{u_r}_{ac}$ of the stability fluctuation given by Eq. (3). To trace the source of this discrepancy, the Fast Fourier Transform (FFT) of the signal $s^{u_r}_{fluc}$ is extracted and plotted in Fig. 9(b). Retrieving the FFT of such signals is difficult to perform because the sampling frequency is quite high in relation to the amplified frequencies. Instead, the peridogram method for power spectrum estimation is used to acquire the frequency signature of the DNS fluctuations. As shown in Fig. 9(b), the main amplified DNS frequency is about $f \approx 335$ Hz. The corresponding intrinsic instability mode appears to be $\omega^0 = 62.787 - 7.389i$, specifically, the mode that precedes the last in Fig. 3 at $X_e = 8$. We posit that this mode, which has a frequency of $f = 333$ Hz, is induced within the DNS computations. This behavior is unexpected because the $f = 333$ Hz frequency lags the natural acoustic frequency by 30 Hz whereas the frequency of the eigenmode introduced here falls within 1 Hz of the natural frequency. A possible explanation is that both eigenmodes are at play.

To identify the stability modes that compose the DNS signal for $s^{u_r}_{fluc}$, a spatial decomposition is performed at each time. The signal from each sensor is assumed to be a combination of the two highest stability modes $\omega^0 = 68.679 - 7.594i$ and $\omega^0 = 62.787 - 7.389i$. The signal is thus determined by the complex amplitude coefficients $A^{68}$ and $A^{62}$ via :

$$s^{u_r}_{fluc} = A^{62}_r \left(\hat{u}^{62}_r\right)_r + A^{62}_i \left(\hat{u}^{62}_r\right)_i + A^{68}_r \left(\hat{u}^{68}_r\right)_r + A^{68}_i \left(\hat{u}^{68}_r\right)_i \tag{11}$$

Using the method of least squares, the coefficients $A^{68}$ and $A^{62}$ are calculated at each time from the whole set of sensor signals for $s^{u_r}_{fluc}$. A linear system in $A^{68}$ and $A^{62}$ is obtained when writing Eq. (11) for the 30 sensors located throughout the chamber. At length, one retrieves the two amplitude coefficients $A^{68}$ and $A^{62}$ that depend on time $t$.

Once these coefficients are known, it remains to be determined whether the same combination of the two stability modes will enable us to accurately predict the axial velocity signal for $s^{u_x}_{fluc}$. To this end, the acoustic parts $s_{ac}^{u_x}$ of $s_{fluc}^{u_x}$ must first be estimated. This requires the use of the coefficients $\{A_m\}$ of the first 100 acoustic modes of Eqs. (4-10) that can be retrieved from a DNS pressure signal, $s_{fluc}^{p} \approx s_{ac}^{p}$ . Then given the function $F_\mu(t)$, the signal $s_{ac}^{u_x}$ can be obtained.

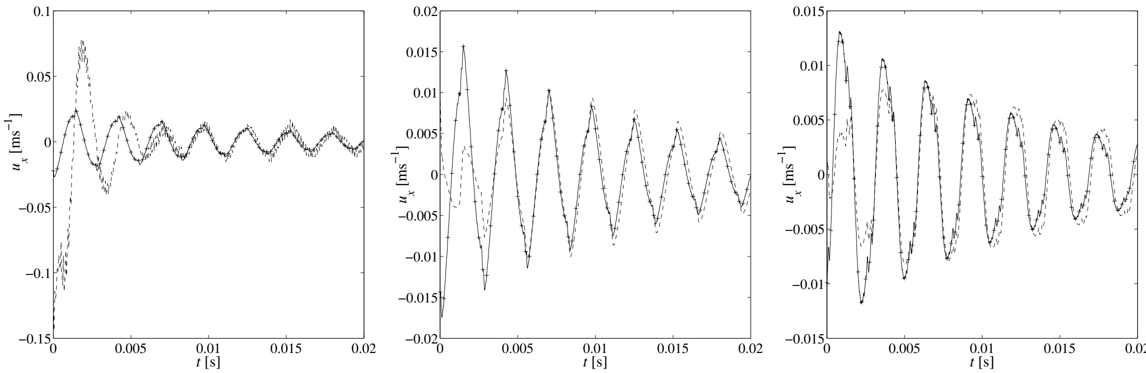

(a) $u_x$ at $(x, r) = (8, 0.866)$ (b) $u_x$ at $(x, r) = (7.333, 0.342)$ (c) $u_x$ at $(x, r) = (6.667, 0.985)$

**Figure 10. Case 3. Comparison between the signals $s_{fluc}^{u_x} - s_{th}^{u_x}$ (dashed lines) and the theoretical acoustic evolution $s_{ac}^{u_x}$ (solid lines with $+$) for three sensors.**

Using the modal decomposition $A^{68}$ and $A^{62}$, one can access the part of the signals due to the stability modes, noted so far as $s_{th}^{u_x}$. To confirm our analysis, we compare in Fig. 10 the vortico-acoustic contribution retrieved from the DNS-based $s_{fluc}^{u_x} - s_{th}^{u_x}$ to the theoretical evolution of vortico-acoustic modes given by $s_{ac}^{u_x}$. The three Figs. 10(a), 10(b), and 10(c) correspond to three distinct sensor locations. The excellent conformity of the two sets of calculations supports the hypothesis that the modal decomposition found from $s_{fluc}^{u_r}$ corresponds to the intrinsic instability contribution to $s_{fluc}^{u_x}$. In other words, the existence in the DNS of the eigenmode $\omega^0 = 62.787 - 7.398i$, not artificially introduced in the computation, is confirmed. This mode has naturally merged in the flow due to the coupling mechanism between the mode $\omega^0 = 68.679 - 7.594i$ and the acoustic modes.

To further explore the interactions between hydrodynamic and acoustic modes, we turn our attention to the amplitude functions, $|A_{62}|$ and $|A_{68}|$, and their respective phase functions, $\varphi^{62} = \arctan\left(A_r^{62}/A_i^{62}\right) = \arg(A^{62})\ [2\pi]$ and $\varphi^{68} = \arctan\left(A_r^{68}/A_i^{68}\right) = \arg(A^{68})\ [2\pi]$. If the DNS calculations had exhibited linear behavior, then the amplitude functions $|A_{62}|$ and $|A_{68}|$ would have matched the theoretical evolutions given by $e^{\nu^{62}t}$ and $e^{\nu^{68}t}$. Similarly, the phase functions $\varphi^{62}$ and $\varphi^{68}$ would have followed the theoretical evolutions $2\pi f^{62}t\ [2\pi]$ and $2\pi f^{68}t\ [2\pi]$. In Figs. 11(a), 11(b), and 11(c), the comparisons of $|A_{62}|$, $|A_{68}|$, $\varphi^{62}$, and $\varphi^{68}$ are provided along with their respective modal evolutions. Graphically, one can see that the introduction of mode $\omega^0 = 68.679 - 7.594i$ has led to the development of mode $\omega^0 = 62.787 - 7.594i$. Rapidly, the mode $\omega^0 = 62.787 - 7.594i$ becomes dominant in the computations, oscillating around a modal evolution curve (see the amplitude function in Fig. 11(a)). Contrary to what is expected, instead of capturing a direct interaction between the stability mode $\omega^0 = 68.679 - 7.594i$ and the first acoustic mode, this DNS calculation suggests the possibility for additional coupling between two neighboring intrinsic instability modes. This is quite interesting because the highest mode $\omega^0 = 68.679 - 7.594i$ is closer to the natural acoustic mode than its nearest neighbor, $\omega^0 = 62.787 - 7.594i$. Instead of intra-coupling between acoustic and stability modes, an interior mode coupling is manifested.

An important mechanism that is discovered here is the possibility for a secondary stability mode to emerge in a flow without being artificially introduced into it. For example, the mode $\omega^0 = 62.787 - 7.594i$ naturally appears in the flow in which a neighboring eigenmode, $\omega^0 = 68.679 - 7.594i$, is imposed.

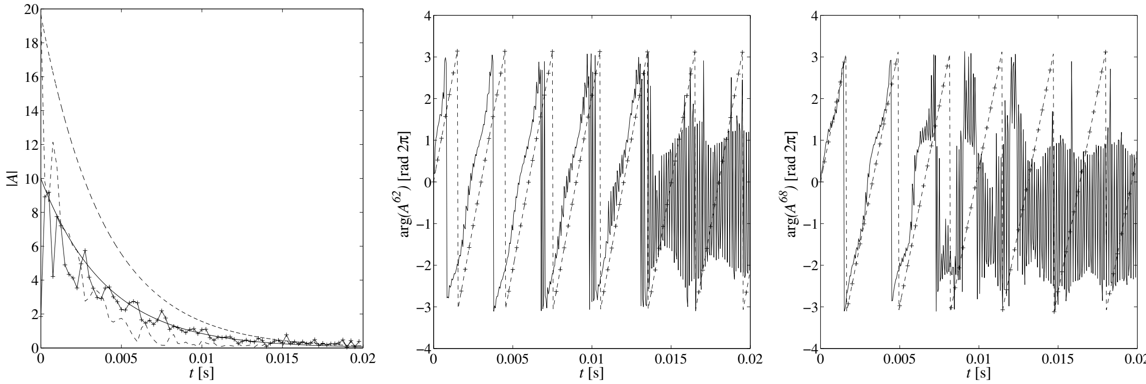


(a) amplitudes $|A_{62}|$ and $|A_{68}|$ (b) $\varphi^{62}$ (c) $\varphi^{68}$

**Figure 11. Case 3. Part 11(a) shows the amplitude evolution for the two modes $\omega = 62.787 - 7.389i$ (solid line with $+$) and $\omega = 68.679 - 7.594i$ (dashed line). These amplitudes are compared to $10e^{\nu^{62}t}$ and $0.01A_0 \parallel \left(\hat{u}_r^{68}\right)_r \parallel_\infty e^{\nu^{68}t}$. Parts 11(b) and 11(c) compare the phase functions $\varphi^{62}$ and $\varphi^{68}$ (dashed lines) to the theoretical evolutions $2\pi f^{62}t\ [2\pi]$ and $2\pi f^{68}t\ [2\pi]$ (solid lines with $+$).**

## V. Conclusions

In this study, we have shown that the use of DNS calculations can provide new physical insight into understanding the results of biglobal stability analysis. For example, we have demonstrated that the critical eigenvalues precipitated by the theoretical stability analysis are recovered when computing the unsteady motion of an isolated fluctuation through DNS calculations. In the process, special attention has been paid to the dependence of the temporal growth rate $\omega_i$ on the chamber length $X_e$. Evidently, $\omega_i$ controls the stability character of these modes. As $\omega_i$ approaches zero with successive increases in $X_e$, one expects that for a sufficiently large value of $X_e$, $\omega_i$ will turn positive, thus changing the temporal character from damping to growth. Under these auspices, fluctuations will become temporally unstable to the extent of increasing in amplitude with the passage of time. Such behavior is found to occur for $X_e > 16$. Interestingly, in cold gas experiments, it has been corroborated that turbulence will ensue for $X_e > 13$. Once the flow becomes turbulent, the linear stability analysis no longer holds. Nonlinear effects will have to be incorporated as they begin to act even as the modes become unstable. Several comparisons with cold[21] and reactive gas experiments[20] have demonstrated the relevance of biglobal stability analyses in accurately estimating the temporally stable modes. The nature of the intrinsic instabilities has also led to a coherent construct that explains the source of SRM thrust oscillations.

In addition to their important role in confirming the biglobal stability results, these DNS calculations have illuminated the quality and accuracy of Majdalani's analytical solution for the vortico-acoustic boundary-driven waves associated with the Taylor-Culick flow. Moreover, we have managed to show that the proximity of instability frequencies to natural acoustic modes can lead to the attraction and merging of neighboring stability modes. Other DNS computations made with unsteady injection velocity have established the presence of strong coupling between acoustic and intrinsic instability modes. For unsteady injection velocity cases, the frequency of one mode $f = V_{inj}\omega_r/(2\pi R)$ becomes a function of the time $t$ and can cross the acoustic mode $f_{ac}$. Thus we reproduce what occurs in live motors where the coupling mechanism between acoustics and intrinsic instabilities is believed to be responsible for the merging of the frequency paths.[21]

## Acknowledgments

This study has been supported by the French Space Agency CNES and by ONERA. The authors thank M. Prévost and G. Avalon from ONERA for their accurate measurements, help, and useful suggestions. J. Majdalani was supported by the National Science Foundation, particularly through a CAREER grant and a supplemental award on International Research and Education in Engineering.

# References

[1]Fabignon, Y., Dupays, J., Avalon, G., Vuillot, F., Lupoglazoff, N., Casalis, G., and Prévost, M., "Instabilities and Pressure Oscillations in Solid Rocket Motors," *Aerospace Science and Technology*, Vol. 7, No. 3, 2003, pp. 191–200.

[2]Ugurtas, B., Avalon, G., Lupoglazoff, N., Vuillot, F., and Casalis, G., "Stability and Acoustic Resonance of Internal Flows Generated by Side Injection," *Solid Propellant Chemistry, Combustion, and Motor Interior Ballistics*, edited by V. Yang, T. B. Brill, and W. Z. Ren, Vol. 185, AIAA Progress in Astronautics and Aeronautics, Washington, DC, 2000, pp. 823–836.

[3]Couton, D., Plourde, F., and Doan-Kim, S., "Cold Gas Simulation of a Solid Propellant Rocket Motor," *AIAA Journal*, Vol. 34, No. 12, 1996, pp. 2514–2522.

[4]Varapaev, V. and Yagodkin, V., "Flow Stability in a Channel with Porous Wall," *Fluid Dynamics (Izv. AN SSSR. Mekhanika Zhidkosi i Gaza.)*, Vol. 4, No. 5, 1969, pp. 91–95.

[5]Beddini, R. A., "Injection Induced Flows in Porous-Walled Ducts," *AIAA Journal*, Vol. 24, No. 11, 1986, pp. 1766–1773.

[6]Lee, Y. and Beddini, R., "Acoustically-Induced Turbulent Transition in Solid Propellant Rocket Chamber Flowfields," *AIAA Paper 99-2508*, June 1999.

[7]Lee, Y. and Beddini, R., "Effect of Solid Rocket Chamber Pressure on Acoustically-Induced Turbulent Transition," *AIAA Paper 2000-3802*, July 2000.

[8]Casalis, G., Avalon, G., and Pineau, J. P., "Spatial Instability of Planar Channel Flow with Fluid Injection through Porous Walls," *Physics of Fluids*, Vol. 10, No. 10, 1998, pp. 2558–2568.

[9]Griffond, J. and Casalis, G., "On the Nonparallel Stability of the Injection Induced Two-Dimensional Taylor Flow," *Physics of Fluids*, Vol. 13, No. 6, 2001, pp. 1635–1644.

[10]Griffond, J., Casalis, G., and Pineau, J. P., "Spatial Instability of Flow in a Semiinfinite Cylinder with Fluid Injection through Its Porous Walls," *European Journal of Mechanics, B/Fluids*, Vol. 19, No. 1, 2000, pp. 69–87.

[11]Griffond, J. and Casalis, G., "On the Dependence on the Formulation of Some Nonparallel Stability Approaches Applied to the Taylor Flow," *Brief Communications in Physics of Fluids*, Vol. 12, No. 2, 2000, pp. 466–468.

[12]Taylor, G. I., "Fluid Flow in Regions Bounded by Porous Surfaces," *Proceedings of the Royal Society, London, Series A*, Vol. 234, No. 1199, 1956, pp. 456–475.

[13]Culick, F., "Rotational Axisymmetric Mean Flow and Damping of Acoustic Waves in a Solid Propellant Rocket," *AIAA Journal*, Vol. 4, No. 8, 1966, pp. 1462–1464.

[14]Vuillot, F., "Vortex Shedding Phenomena in Solid Propellant Motors," *Journal of Propulsion and Power*, Vol. 11, No. 4, 1995, pp. 626–639.

[15]Couton, D., Doan-Kim, S., and Vuillot, F., "Numerical Simulation of Vortex-Shedding Phenomenon in a Channel with Flow Induced through Porous Wall," *International Journal of Heat and Fluid Flow*, Vol. 18, No. 3, 1997, pp. 283–296.

[16]Ugurtas, B., Avalon, G., Lupoglazoff, N., and Vuillot, F., "Numerical Computations of Hydrodynamic Instabilities inside Channels with Wall Injection," *AIAA Paper 99-2505*, June 1999.

[17]Avalon, G., Casalis, G., and Griffond, J., "Flow Instabilities and Acoustic Resonance of Channels with Wall Injection," *AIAA Paper 98-3218*, July 1998.

[18]Abu-Irshaid, E., Majdalani, J., and Casalis, G., "Hydrodynamic Stability of Rockets with Headwall Injection," *Physics of Fluids*, Vol. 19, No. 2, 2007, pp. 024101–11.

[19]Chedevergne, F. and Casalis, G., "Thrust Oscillations in Reduced Scale Solid Rocket Motors, Part II : a Theoretical Approach," *AIAA Paper 2005-4000*, July 2005.

[20]Chedevergne, F. and Casalis, G., "Detailed Analysis of the Thrust Oscillations in Reduced Scale Solid Rocket Motors," *AIAA Paper 2006-4424*, 2006.

[21]Chedevergne, F., Casalis, G., and Féraille, T., "Biglobal Linear Stability Analysis of the Flow Induced by Wall Injection," *Physics of Fluids*, Vol. 18, No. 1, 2006, pp. 014103–14.

[22]Prévost, M. and Godon, J.-C., "Thrust Oscillations in Reduced Scale Solid Rocket Motors, Part I : Experimental Investigations," *AIAA Paper 2005-4003*, July 2005.

[23]Avalon, G., "Private Communication," April 2006.

[24]Majdalani, J. and Moorhem, W. V., "Improved Time-Dependent Flowfield Solution for Solid Rocket Motors," *AIAA Journal*, Vol. 36, No. 2, 1998, pp. 241–248.

[25]Majdalani, J., "The Boundary Layer Structure in Cylindrical Rocket Motors," *AIAA Journal*, Vol. 37, No. 4, 1999, pp. 505–508.

[26]Majdalani, J., "The Oscillatory Channel Flow with Arbitrary Wall Injection," *Journal of Applied Mathematics and Physics (ZAMP)*, Vol. 52, No. 1, 2001, pp. 33–61.

[27]Majdalani, J. and Flandro, G., "The Oscillatory Pipe Flow with Arbitrary Wall Injection," *Proceedings of the Royal Society, London, Series A*, Vol. 458, No. 2022, 2002, pp. 1621–1651.

[28]Chedevergne, F. and Casalis, G., "Front Wall Boundary Layer Influence on the Stability of the Flow Induced by Wall Injection," $7^{th}$ *ONERA DLR Aerospace Symposium*, Toulouse, France, 4-6 October 2006.

[29]Majdalani, J., "On Steady Rotational High Speed Flows : the Compressible Taylor-Culick Profile," *Proceedings of the Royal Society, London, Series A*, Vol. 463, No. 2077, 2007, pp. 131–162.

[30]Theofilis, V., "Advances in Global Linear Instability Analysis of Nonparallel and Three-Dimensional Flows," *Progress in Aerospace Sciences*, Vol. 39, No. 2, 2003, pp. 249–315.

[31]Casalis, G., Chedevergne, F., Féraille, T., and Avalon, G., "Global Stability of the Flow Induced by Wall Injection," *IUTAM,Symposium on Laminar-Turbulent Transition*, Bangalore, India, December, 13-17 2004.

[32]Golub, G. and Loan, C. V., *Matrix Computations (Third Edition)*, The Johns Hopkins University Press, 1996.

[33]Chevalier, P., Courbet, B., Dutoya, D., Klotz, P., Ruiz, E., Troyes, J., and Villedieu, P., "CEDRE : Development and Validation of a Multiphysic Computational Software," *1st European Conference for Aerospace Sciences (EUCASS)*, Moscow, Russia, 2005.

[34]Vuillot, F., Scherrer, D., and Habiballah, M., "CFD Code Validation for Space Propulsion Applications," *5th International Symposium on Liquid Space Propulsion*, Chattanooga, Tennessee, 2003.

[35]Apte, S. and Yang, V., "Unsteady Flow Evolution in a Porous Chamber with Surface Mass Injection, Part I : Free Oscillation," *AIAA Journal*, Vol. 39, No. 8, 2001, pp. 1577–1586.

[36]Apte, S. and Yang, V., "Unsteady Flow Evolution in Porous Chamber with Surface Mass Injection, Part II : Acoustic Excitation," *AIAA Journal*, Vol. 40, No. 2, 2001, pp. 244–253.

[37]Chu, B.-T. and Kovásznay, L., "Non-Linear Interactions in a Viscous Heat-Conducting Compressible Gas," *Journal of Fluid Mechanics*, Vol. 3, No. 5, 1958, pp. 494–514.

[38]Griffond, J., "Receptivity and Aeroacoustic Resonance in Channels with Blowing Walls," *Physics of Fluids*, Vol. 14, No. 11, 2002, pp. 3946–3962.

[39]Majdalani, J., "A Hybrid Multiple Scale Procedure for Boundary Layers Involving Several Dissimilar Scales," *Journal of Applied Mathematics and Physics (ZAMP)*, Vol. 49, No. 6, 1998, pp. 849–868.

[40]Wasistho, B., Balachandar, S., and Moser, R., "Compressible Wall-Injection Flows in Laminar, Transitional, and Turbulent Regimes : Numerical Prediction," *Journal of Spacecraft and Rockets*, Vol. 41, No. 6, 2004, pp. 915–924.